Research Square

Preprints are preliminary reports that have not undergone peer review.
They should not be considered conclusive, used to inform clinical practice,
or referenced by the media as validated information.

Effect of Spatial Stiffness Variability in CDM-Improved Ground on Retaining Wall Displacement

Trong Nghia Le

letrongnghia@hcmut.edu.vn

Ho Chi Minh City University of Technology

Khac Tan Da Nguyen

Ho Chi Minh City University of Technology

Huynh Huy Nguyen

Ho Chi Minh City University of Technology

Minh Trung Nguyen

Ho Chi Minh City University of Technology

Trung Kien Nguyen

Ho Chi Minh City University of Technology

Research Article

Keywords: Deep excavation, Random field, Monte Carlo simulation, Cement deep mixing

Posted Date: November 16th, 2026

DOI: https://doi.org/10.21203/rs.3.rs-11611472/v1

License: This work is licensed under a Creative Commons Attribution 4.0 International License.
Read Full License

Additional Declarations: No competing interests reported.

Effect of Spatial Stiffness Variability in CDM-Improved Ground on Retaining Wall Displacement

ABSTRACT

Cement deep mixing (CDM)-improved ground is often modeled using uniform properties, although its stiffness varies spatially. This study examines how this variability affects wall displacement in a soft-ground excavation in Ho Chi Minh City, Vietnam. The excavation was supported by a CDM retaining wall and a CDM-improved base. A two-dimensional finite-element model was calibrated against inclinometer measurements. Tests on 578 specimens from 65 field columns yielded a mean secant modulus E50 of 956.61 MPa and a coefficient of variation (COV) of 0.53. Lognormal stiffness fields were generated using spectral representation and assigned to the equivalent material representing the improved base. Wall properties and material strengths were held constant. The baseline analysis included 300 realizations. Six additional cases, each with 50 realizations, examined changes in COV and the horizontal and vertical scales of fluctuation. The baseline displacements formed two clusters around 8.5-8.6 mm and 9.5-9.6 mm. A two-component lognormal mixture was fitted to this distribution. Increasing COV from 0.1 to 0.3 increased the displacement standard deviation from 0.085 to 0.26 mm, with little change in the mean. Changes in the scales of fluctuation also affected dispersion. The probability of exceeding the measured displacement of 8.84 mm was approximately 44% in the baseline case and 42-52% in the parametric cases. These values represent the probability of exceeding a field-measured displacement, not the probability of structural failure. The results show that base-stiffness variability can affect displacement dispersion more than the mean response within the investigated ranges. Their interpretation remains subject to the equivalent-continuum assumptions and finite Monte Carlo sample sizes.

Keywords: Deep excavation, Random field, Monte Carlo simulation, Cement deep mixing.

1. INTRODUCTION

Deep excavations in soft ground can experience substantial wall deformation because the surrounding soils often exhibit low shear strength and high compressibility. Cement Deep Mixing (CDM) is widely used for ground improvement and can also form part of an excavation retaining system [1-4]. Previous field, numerical, and experimental studies have shown that CDM wall behavior depends on wall configuration, material properties, excavation depth, and construction sequence [2-5].

Conventional numerical analyses generally represent CDM-treated materials using deterministic properties based on representative or mean values. This approach is convenient but does not capture the inherent heterogeneity of deep-mixed materials. Field and laboratory studies have reported considerable variability in deep-mixed column properties because of differences in soil conditions, binder distribution, and mixing quality [6]. Reliability studies have also shown that spatial variability in deep-mixed ground can influence deformation and system performance [7]. Pan et al. [8] reported similar effects for cement-treated soil beneath a deep excavation. These findings suggest that analyses based only on mean properties may not adequately represent unfavorable local conditions or the full range of possible excavation responses.

Random field theory provides a practical framework for representing both statistical variability and spatial correlation in geotechnical properties [9]. Its use in deep-excavation analysis has increased in recent years, particularly for deformation and reliability assessment [10,11]. Luo et al. [10] demonstrated that spatial variability in soft-clay properties can affect the serviceability performance of braced excavations. Nguyen and Le [12] later applied a two-dimensional random field to jet-grouted ground in a field-calibrated deep-excavation model. Their study quantified the influence of spatially variable stiffness on diaphragm-wall displacement and displacement-exceedance probability [12]. Nevertheless, most random-field studies of excavations have focused on natural soil, rock, or other forms of treated ground [10-12]. Comparatively fewer studies have examined spatial variability within CDM-improved ground acting together with a CDM retaining wall. In particular, the influence of E_{50} variability, COV, and spatial correlation on CDM wall displacement remains insufficiently quantified.

This study investigates these issues using a two-dimensional random finite-element framework for a field deep excavation supported by a CDM retaining wall and internally improved with CDM. The deterministic finite-element model was calibrated against the displacement profile measured at inclinometer P07. Site-specific statistical information is obtained from 578 specimens collected from 65 field CDM columns. The secant modulus E_{50} of the CDM-improved zone is then modeled as a spatially variable lognormal random field. The present analysis focuses on the spatial variability of E_{50}, while the other CDM properties are retained at their representative values. Monte Carlo simulations are used to obtain the distribution of CDM retaining-wall displacement. The effects of COV and the horizontal and vertical scales of fluctuation, θ_x and θ_y, are subsequently examined. The probability of exceeding the observed maximum wall displacement of 8.84 mm is also evaluated. The main contribution is the integration of a field-calibrated excavation model with site-specific CDM variability in a probabilistic framework. This approach quantifies how spatial

variability in CDM stiffness can alter wall displacement beyond predictions based on uniform mean properties.

2. BACK-ANALYSIS OF CDM RETAINING-WALL DISPLACEMENT

2.1. Project Description

This study based on Phase 1C of the Riviera Point mixed-use residential and commercial development in Tan Phu Ward, District 7, Ho Chi Minh City, Vietnam, which was constructed by Coteccons Construction Joint Stock Company [13]. The project comprises one basement level, with excavation depths varying across the site from approximately -3.6 m to -5.5 m, as shown in Fig. 1. Construction was carried out using the bottom-up method. This project provides a practical case for investigating the influence of spatial variability in CDM-improved ground on excavation-induced wall displacement.

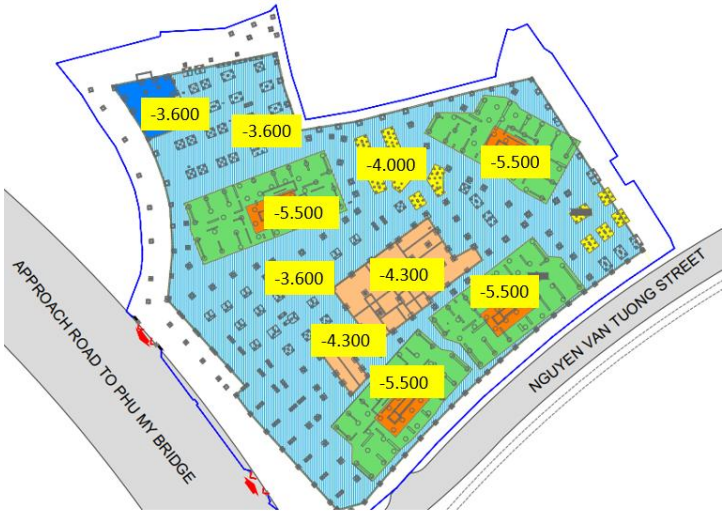


Fig. 1 Site plan and excavation levels of the Riverpoint 1C project [13].

The site is underlain by a thick deposit of soft to very soft clay, as shown in **Fig. 2**. The natural unit weight of the clay is approximately 14-16 kN/m³, while the natural water content generally exceeds the plastic limit and is close to or above the liquid limit. The SPT *N*-values remain close to zero within the upper 10 m and gradually increase with depth to about 4 near 20 m. The undrained shear strength s_u is generally around 20 kPa within the upper 12 m and increases with depth to approximately 45 kPa near 20 m.

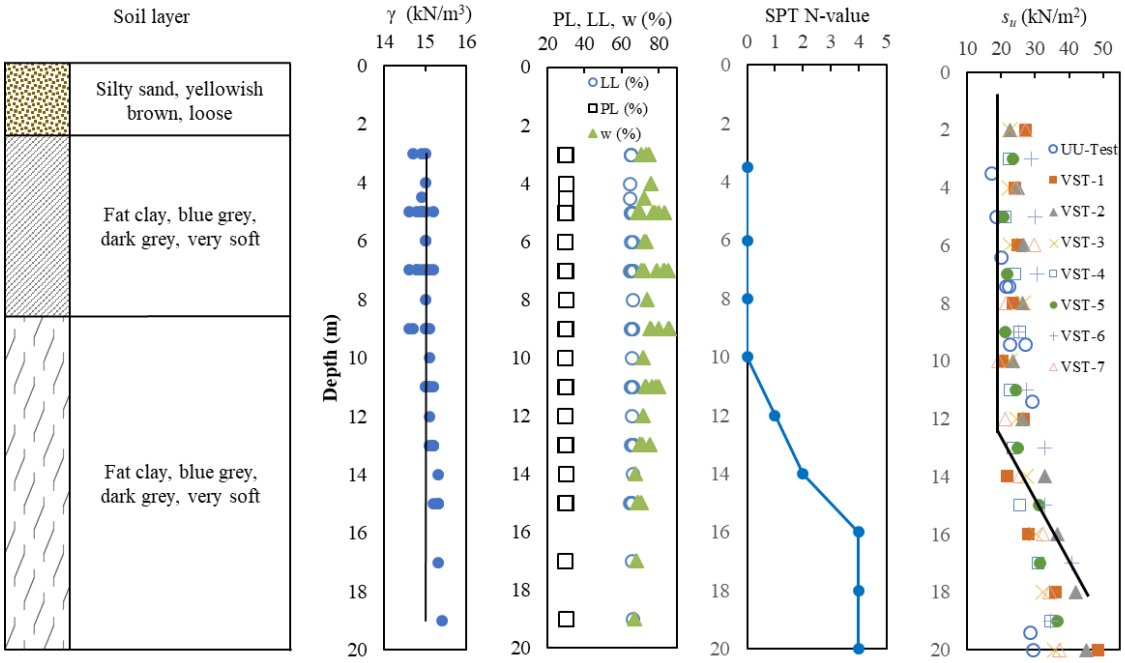


Fig. 2 Subsoil profile and selected geotechnical properties at the project site.

The construction sequence is illustrated in **Fig. 3**. CDM columns were installed first (**Fig. 3a**), followed by excavation to the design levels of the basement floor, foundation base, and water tank bottom (**Fig. 3b**). The basement structure was then constructed.

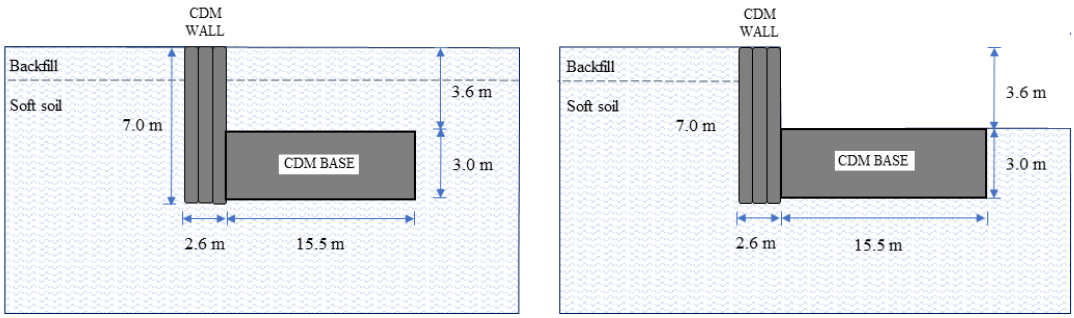


Fig. 3 Construction sequence of the deep excavation: (a) installation of CDM columns; (b) excavation to the design elevation of the basement floor.

Fig. 4 shows the plan layout of CDM improvement ratios and the locations of 32 inclinometers used to monitor CDM wall displacement. CDM was used both as a perimeter retaining wall and for ground improvement within the excavation. The retaining wall comprised two to six rows of CDM columns, depending on location. The wall extended to depths of 7-9 m, with improvement ratios ranging from 75% to 95%. Within the excavation, the CDM-improved zone extended to depths of 3-5 m, with improvement ratios of 22%-27%.



Fig. 4 Plan layout of CDM improvement ratios and inclinometer locations at the project site.

2.2. Calibration of the Excavation Model Against Inclinometer Measurements

Soil Model and Parameters

PLAXIS 2D was used to back-analyze the excavation sequence at Section 4-4, corresponding to inclinometer P07 in **Fig. 4**. The Hardening Soil (HS) model was adopted for the fill and Layers 2a and 2b. The model accounts for stress-dependent stiffness and distinguishes between primary loading and unloading-reloading behavior [14]. The adopted soil parameters are summarized in **Table 1**.

The effective strength parameters c' and φ' were obtained from consolidated-undrained (CU) triaxial tests. In the HS model, E_{50}^{ref} represents the reference secant stiffness at 50% mobilization of the maximum shear strength in a standard triaxial test [14]. The reference stress p^{ref} was set to 100 kPa. For clayey soils, E_{50}^{ref} is commonly estimated from empirical correlations with the undrained shear strength s_u [14,15]. Empirical relationships of $E_{50} = 300s_u$ for soft clay and $E_{50} = 500s_u$ for stiff clay have been used in numerical analyses of deep excavations in Ho Chi Minh City [16].

The parameter E_{oed}^{ref} denotes the reference tangent stiffness for primary oedometer loading, whereas E_{ur}^{ref} represents the unloading-reloading stiffness [14]. In the absence of direct stiffness measurements, $E_{oed}^{ref} = E_{50}^{ref}$ and $E_{ur}^{ref} = 3E_{50}^{ref}$ were adopted in the present model [16,17].

Table 1. Selected soil input parameters used in the Hardening Soil model.

Soil layer	F	2a	2b
Thickness (m)	2.1	4	6
Drainage type	Drained	Undrained A	Undrained A

Unsaturated unit weight γ_{unsat} (kN/m^3)	18	14.9	15.3
Saturated unit weight γ_{sat} (kN/m^3)	18	15	15.5
E_{50}^{ref} (kPa)	30000	13000	14200
E_{oed}^{ref} (kPa)	30000	13000	14200
E_{ur}^{ref} (kPa)	90000	39000	42600
Effective cohesion c' (kPa)	5	9.92	9.2
Effective friction angle φ' (°)	30	23	25.4

CDM properties

At a curing age of 28 days, 65 CDM columns, representing approximately 1% of all constructed columns, were randomly selected for quality evaluation. A total of 578 specimens were subjected to unconfined compression tests. The secant modulus E_{50} was determined from the axial stress-strain curve as the ratio of the stress at 50% of the peak compressive strength to the corresponding axial strain. **Fig. 5** illustrates the variations in unconfined compressive strength q_u and secant modulus E_{50} with depth. Both parameters exhibit considerable scatter, with no clear increasing or decreasing trend with depth. Their statistical characteristics, including the mean, standard deviation, and coefficient of variation (COV), are summarized in Table 2.

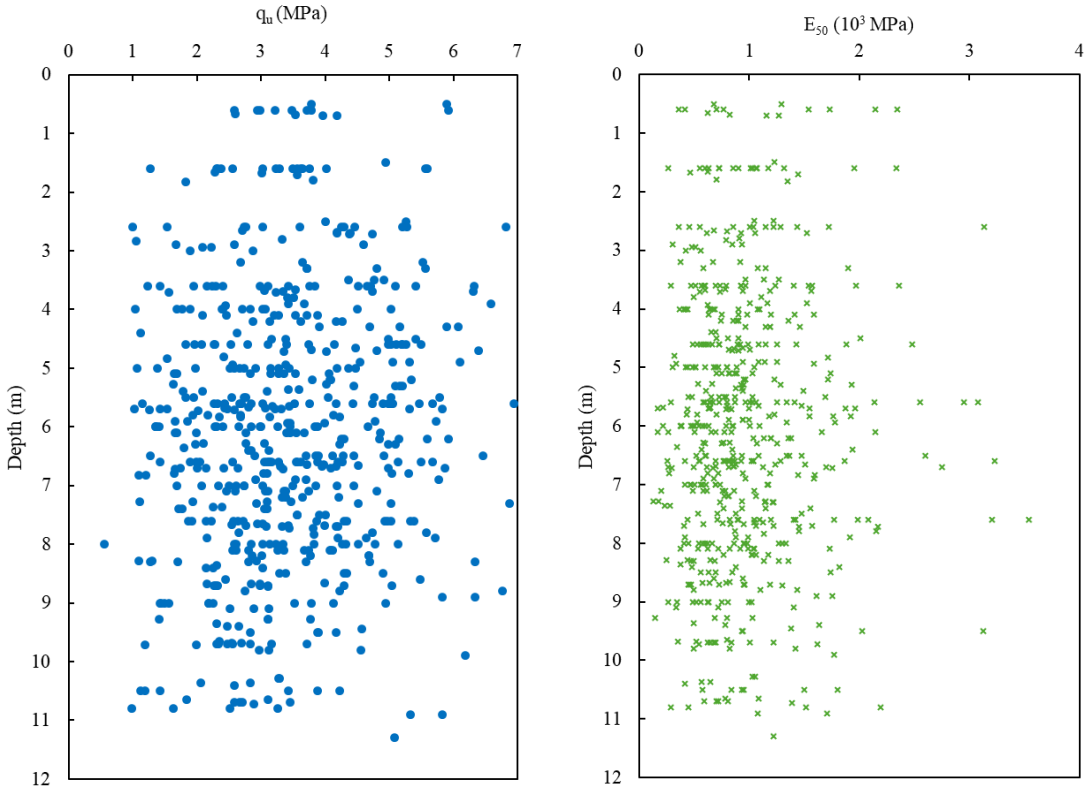


Fig. 5 Variation of unconfined compressive strength q_u and secant modulus E_{50} with depth**.**

To quantify the variability in the mechanical properties of the CDM-treated soil, the sample mean, standard deviation, and coefficient of variation (COV) were calculated from the experimental data. The sample

standard deviation was estimated using the (n-1) denominator, while the COV was defined as the ratio of the sample standard deviation to the sample mean [18, 19]. As summarized in Table 2, the mean values of q_u and E_{50} are 3.40 and 956.61 MPa, respectively, with corresponding standard deviations of 1.26 and 509.88 MPa. The COV of E_{50} (0.53) is higher than that of q_u (0.37), indicating greater relative variability in the secant modulus.

Table 2. Statistical characteristics of unconfined compressive strength q_u and secant modulus E_{50} of CDM specimens.

Parameter	Mean μ_x (MPa)	Standard deviation σ_x (MPa)	COV
E_{50}	956.61	509.88	0.53
q_u	3.40	1.26	0.37

Different constitutive models were adopted for the two CDM-reinforced zones based on their area replacement ratios and structural functions. The CDM retaining wall was represented by a linear elastic equivalent material, with an adopted area replacement ratio of 75%. This idealization was used to examine wall displacement under the assumption that material failure does not occur. It does not simulate cracking, stiffness degradation, or post-failure behavior of the CDM wall. In contrast, the excavation-base improvement zone, with a lower replacement ratio of 22%, was modeled using the Mohr-Coulomb model to account for both stiffness and shear strength of the equivalent CDM-soil composite. The Mohr-Coulomb model has also been used to represent cement-treated material in numerical analyses of DCM retaining walls in soft clay [3].

In the PLAXIS 2D model, the CDM columns and intervening soil were represented by equivalent continuum materials rather than individual columns. Their stiffness was estimated using an area-weighted approximation based on the laboratory CDM modulus and the area replacement ratio. This approach assumes compatible deformation of the CDM and untreated soil and does not explicitly represent column-soil relative movement or the three-dimensional column arrangement.

The unconfined compression tests yielded mean values of q_u = 3.40 MPa and E_{50} = 956.61 MPa, as summarized in **Table 2**. The measured E_{50} was used as a representative stiffness to calculate the equivalent Young's moduli assigned to the Linear Elastic and Mohr-Coulomb materials. This approximation does not account for variations in CDM stiffness with stress level or strain. The equivalent Young's modulus of each reinforced zone was estimated using an area-weighted approach in Eq (1) [20]:

$$E_{eq} = aE_{CDM} + (1-a)E_{soil} \quad (1)$$

where (a) is the CDM area replacement ratio, and E_{CDM} and E_{soil} are the Young's moduli of the CDM material and untreated soil, respectively.

Because the untreated soft clay was substantially less stiff than the CDM material, its contribution to the equivalent stiffness was neglected, giving $E_{eq} \approx aE_{CDM}$. At Section 4-4, the retaining wall comprised

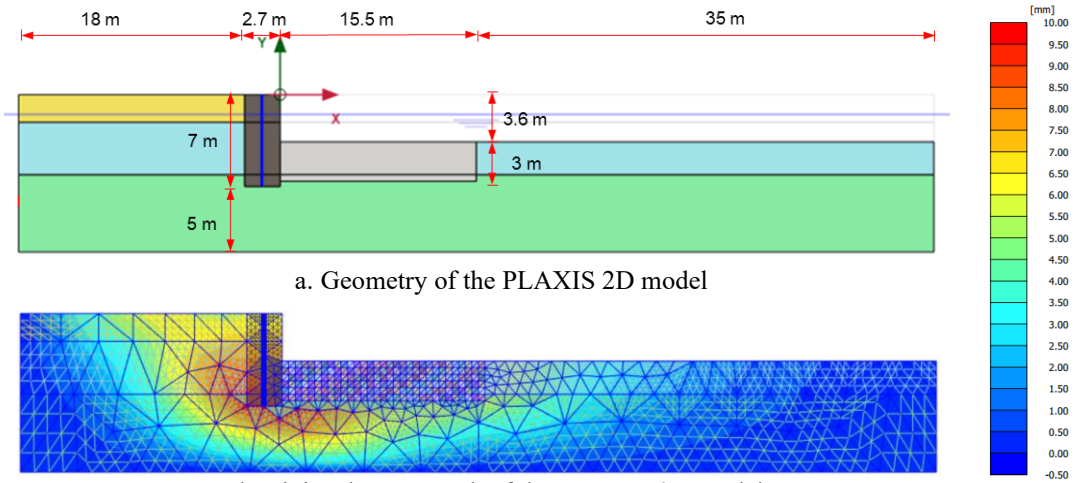
overlapping soil-cement columns with untreated soil remaining between them, while the excavation-base improvement comprised intersecting strips of CDM columns forming a grid. Area replacement ratios of 75% and 22% were adopted in the numerical model for the retaining wall and the excavation-base improvement zone, respectively. The corresponding equivalent Young's moduli were approximately 717 and 210 MPa. These moduli represent the equivalent CDM-soil materials rather than individual columns. The area-weighted approximation does not explicitly account for directional differences in composite stiffness or variations in load transfer between the columns and surrounding soil.

The equivalent undrained shear strength of the excavation-base improvement zone was estimated from the mean unconfined compressive strength. Assuming $s_u = q_u/2$ and neglecting the shear resistance of the untreated soft clay, the equivalent strength was calculated using $s_u = aq_u/2$. With an area replacement ratio of 22% and a mean UCS of 3.40 MPa, the equivalent undrained shear strength was estimated to be 374 kPa. This value represents a simplified area-weighted strength of the homogenized material rather than the measured strength of an individual CDM column. This approximation does not explicitly account for local failure or differences in strain mobilization between the CDM columns and the surrounding soil.

The retaining wall was assigned a non-porous linear elastic model, whereas the CDM-improved ground was represented by the Mohr-Coulomb model with Undrained B behavior. The adopted constitutive models and equivalent material parameters are summarized in Table 3. **Fig. 6** shows the geometry and dimensions of the PLAXIS 2D model used for the back-analysis of Section 4-4 at inclinometer P07. Horizontal displacement was restrained along the vertical boundaries, while both horizontal and vertical displacements were restrained at the bottom boundary. The initial stresses were generated using the K_0 procedure.

Table 3. Constitutive models and material parameters adopted for CDM elements in the numerical analysis.

Material	Constitutive model	Drainage type	E_{eq} (kPa)	s_u (kPa)
CDM wall (75%)	Linear elastic	Non-porous	717,000	-
CDM-improved ground (22%)	Mohr-Coulomb	Undrained B	210,000	374



a. Geometry of the PLAXIS 2D model

b. Finite element mesh of the PLAXIS 2D model

Fig. 6 Geometry and finite element mesh of the PLAXIS 2D model used for the back-analysis of Section 4-4

Lateral displacement measurements from 32 inclinometers were reviewed to assess the deformation response of the CDM retaining wall. Ten monitoring locations (P01, P04, P05, P06, P07, P08, P09, P14, P15, and P32) were selected because their CDM configurations were comparable to that of Section 4-4, particularly in terms of the area replacement ratio and the extent of ground improvement within the excavation. As shown in **Fig. 7**, the measured displacement profiles exhibit similar trends, with lateral displacement generally increasing with depth and reaching its maximum near the wall toe at approximately 7.0 m. Inclinometer P07, located at Section 4-4, recorded the largest displacement of 8.84 mm and was therefore selected as the reference for back-analysis.

The calibrated PLAXIS 2D model predicted a maximum lateral displacement of 8.86 mm, compared with 8.84 mm measured at P07, corresponding to a difference of 0.02 mm (0.23%). The calculated profile also reproduced the general variation of displacement with depth. Because the P07 measurements were used for calibration, this agreement should not be interpreted as independent validation. The other nine inclinometer profiles provide field context for locations with comparable CDM configurations, but do not independently validate the Section 4-4 model. The calibrated model was subsequently used as the reference for the random-field analyses.

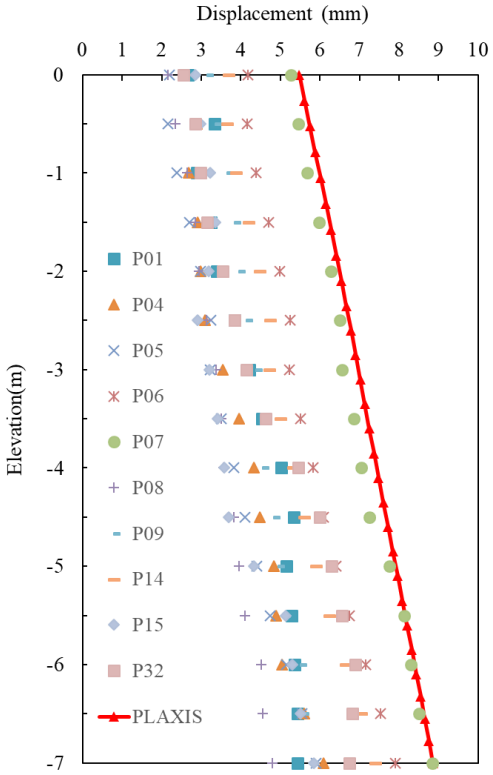


Fig. 7 Comparison of measured and PLAXIS 2D-predicted lateral displacements of the CDM retaining wall.

3. RANDOM FINITE ELEMENT METHODOLOGY

3.1. Random Field Generation and FEM Implementation

The spatial variability of the CDM secant modulus E_{50} was considered in the random finite element analysis, while the unconfined compressive strength q_u and other material properties were kept at their representative values. The measured mean and coefficient of variation (COV) of E_{50} were 956.61 MPa and 0.53, respectively (**Table 2**). Since the secant modulus is strictly positive, a lognormal distribution was adopted to characterize its inherent variability. This choice is consistent with previous probabilistic studies [21, 22], which used lognormal distributions to avoid physically unrealistic negative values of geotechnical parameters. The spatially correlated random fields were generated using the spectral representation method of Shinozuka and Deodatis [23].

The random field was applied to the CDM-improved ground beneath the excavation, while the retaining-wall properties remained deterministic. As shown in **Fig. 8**, the improved zone was represented by a two-dimensional domain measuring 15.5 m × 3.0 m, divided into 31 × 6 cells of 0.5 m × 0.5 m. Each cell was assigned equivalent CDM-soil material properties rather than representing an individual CDM column. Stiffness variations between the columns and untreated soil within each cell were therefore not explicitly modeled. The CDM-soil stiffness E_{50} was selected as the spatially variable parameter, while the remaining material parameters were kept deterministic. A standard Gaussian random field Z(x,y), with zero mean and unit variance N(0,1) was then generated for E_{50} over the discretized domain. An anisotropic exponential

autocorrelation function was adopted to impose the prescribed spatial correlation structure on the Gaussian random field, following previous studies [24, 25], as expressed in Eq. (2).

$$\rho(\Delta x, \Delta y) = exp\left(-\frac{2|\Delta x|}{\theta_x} - \frac{2|\Delta y|}{\theta_y}\right) \quad (2)$$

where Δx and Δy are the horizontal and vertical separation distances, respectively, and θ_x and θ_y are the prescribed scales of fluctuation of the Gaussian field. For the exponential correlation model, the scale of fluctuation is defined as twice the integral of the one-dimensional autocorrelation function over positive separation distances.

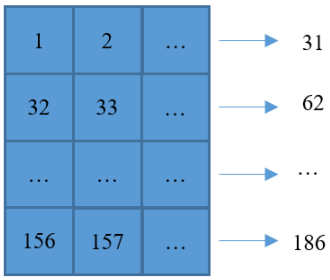


Fig. 8 Discretization of the random-field domain into 31 × 6 cells.

The spectral representation method was used to generate a Gaussian random field from the prescribed spectral density and uniformly distributed random phase angles. Following the approach adopted in previous studies [26, 27], the Gaussian field was subsequently transformed into a lognormal random field. The transformation was performed using Eqs. (3) -(5):

$$E_{50}(x, y) = exp\left[\mu_{\ln E_{50}} + \sigma_{\ln E_{50}} Z(x, y)\right] \quad (3)$$

$$\sigma_{\ln E_{50}} = \sqrt{\ln(1 + COV^2)} \quad (4)$$

$$\mu_{\ln E_{50}} = \ln\left(\mu_{E_{50}}\right) - \frac{\sigma^2_{\ln E_{50}}}{2} \quad (5)$$

where $Z(x,y)$ is a standard Gaussian random field with zero mean and unit variance; $\mu_{\ln E}$ and $\sigma_{\ln E}$ are the mean and standard deviation of the underlying normal distribution, respectively; and $\mu_{E_{50}}$ and COV denote the measured mean and coefficient of variation of the CDM secant modulus, respectively. The modulus values were expressed numerically in MPa when evaluating the logarithmic parameters.

For each realization, the spatial variability of the CDM modulus field was considered in the numerical analysis. The area replacement ratio was kept constant across all realizations, while the stiffness contribution of the untreated soil was neglected, consistent with the deterministic homogenization approach.

3.2. Estimation of Spatial Scales of Fluctuation

The vertical scale of fluctuation of the CDM secant modulus was estimated using Vanmarcke's mean-crossing method [28]. As illustrated in Fig. 9, the distances between successive crossings of the representative E_{50} profiles and their respective mean lines were measured and averaged. The vertical scale of fluctuation was approximated as $\theta_y = 0.8\bar{d}$, where $\bar{d}$ is the mean crossing interval, giving $\theta_y = 1.4$ m.

The available data were insufficient to estimate the horizontal scale of fluctuation directly. A horizontal-to-vertical scale-of-fluctuation ratio of five was assumed, giving $\theta_x = 7.0$ m. This ratio was treated as a modeling assumption, and the influence of the prescribed spatial scales was examined through the parametric analyses. The estimated vertical scale and the assumed horizontal scale were adopted directly as correlation parameters for the underlying Gaussian field. This is an approximation because the exponential transformation changes the normalized autocorrelation function. Consequently, the scales of fluctuation of the resulting lognormal stiffness field are not exactly equal to those prescribed for the Gaussian field.

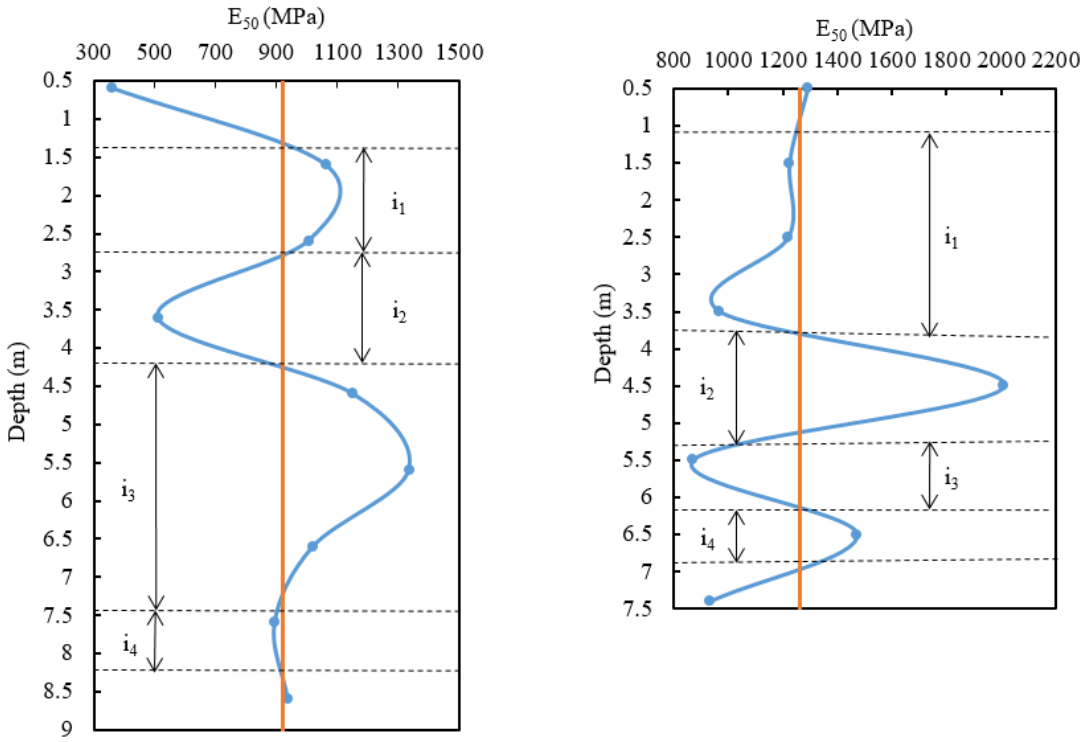


Fig. 9 Estimation of the vertical scale of fluctuation θ_y from representative E_{50} profiles.

3.3. Monte Carlo Simulation and Convergence Assessment

To account for the spatial variability of the secant modulus of CDM soil, a random field of E_{50} was generated using a Python-based procedure implemented in Google Colab. The input parameters are summarized in **Table 4**. The mean E_{50} and coefficient of variation (COV) were specified as 956.61 MPa and 0.53, respectively. Spatial correlation was represented by the exponential autocorrelation model in Eq. (2), with horizontal and vertical scales of fluctuation of 7.0 m and 1.4 m, respectively. The random-field

domain was defined as 15.5 m × 3 m and discretized at intervals of 0.5 m in both directions. These parameters were used to generate spatially variable E_{50} fields for subsequent finite-element analyses in PLAXIS.

Table 4. Input parameters for the random field of the CDM secant modulus

Parameters	Value	Description
$\mu_{E_{50}}$	956.61 MPa	Mean secant modulus
$COV_{E_{50}}$	0.53	Coefficient of variation
$\sigma_{E_{50}}$	509.88 MPa	Standard deviation
θ_x	7.0 m	Horizontal scale of fluctuation
θ_y	1.4 m	Vertical scale of fluctuation
Autocorrelation	Exponential	Spatial correlation structure
L_x	15.5 m	Horizontal extent of the random-field domain
L_y	3 m	Vertical extent of the random-field domain
Δx	0.5 m	Horizontal discretization interval
Δy	0.5 m	Vertical discretization interval

Monte Carlo convergence was assessed using the maximum lateral wall displacement, δ_{max}, which occurred at the wall toe. For each sample size n, the cumulative sample mean and variance of δ_{max} were calculated from the first n random finite element method (RFEM) realizations. The relative changes between consecutive estimates were evaluated using the convergence ratio (CR) defined in Eq. (6) [7,29]:

$$CR_n = \frac{|IM_{n+1} - IM_n|}{IM_n} \times 100\% \quad (6)$$

where IM_n denotes either the cumulative sample mean or the cumulative sample variance of δ_{max} calculated from n realizations. As shown in **Fig. 10**, the convergence ratios of the cumulative mean and variance generally decreased with increasing sample size and remained below 5% from approximately 50 realizations onward in the examined baseline sequence. This indicates smaller changes between successive estimates, but does not establish their statistical precision. The baseline analysis used 300 realizations, whereas the parametric cases used 50 realizations each and were interpreted as exploratory comparisons.

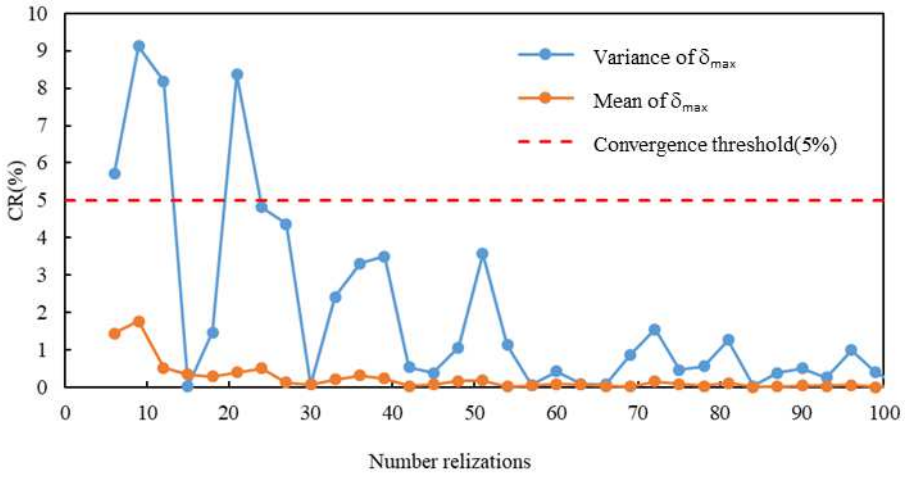


Fig. 10 Convergence ratios of the cumulative mean and variance of the maximum lateral wall displacement with increasing numbers of RFEM realizations.

4. RESULTS AND DISCUSSION

4.1. Effect of spatial variability

Fig. 11 illustrates the implementation of the generated random field in PLAXIS 2D. The random field was assigned to the corresponding material clusters within the excavation-base improvement zone. The retaining-wall properties and other model parameters were kept constant across all realizations. Consequently, the subsequent RFEM analyses isolate the influence of spatial variability in the stiffness of the CDM-improved ground on the predicted wall displacement.

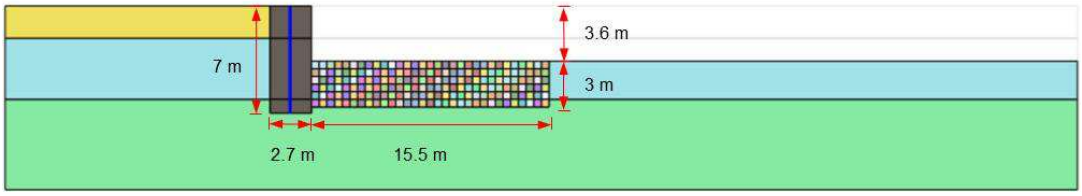
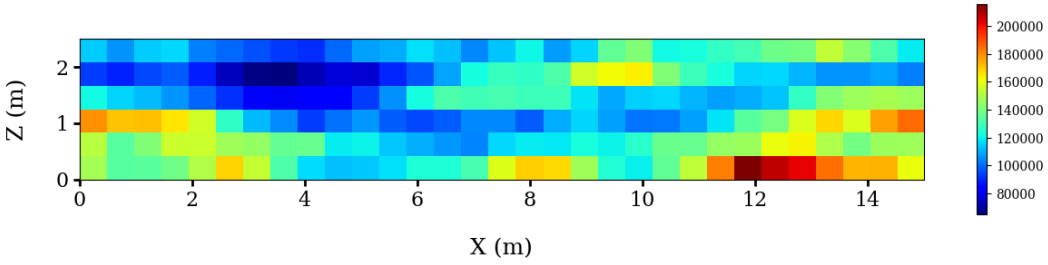
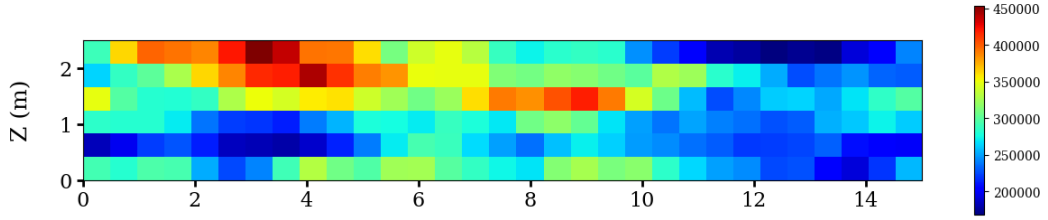


Fig. 11 Implementation of the generated random field in the CDM-improved zone of the PLAXIS 2D model.

Fig. 12 shows the stiffness fields associated with the largest and smallest maximum wall displacements among the 300 realizations, corresponding to Seeds 97 and 251, respectively. Although both fields were generated using the same prescribed statistical parameters, their realized mean stiffnesses and spatial distributions may differ over the finite domain. The displacement difference therefore cannot be attributed solely to the arrangement of weak and stiff zones without examining the statistics of the two fields.



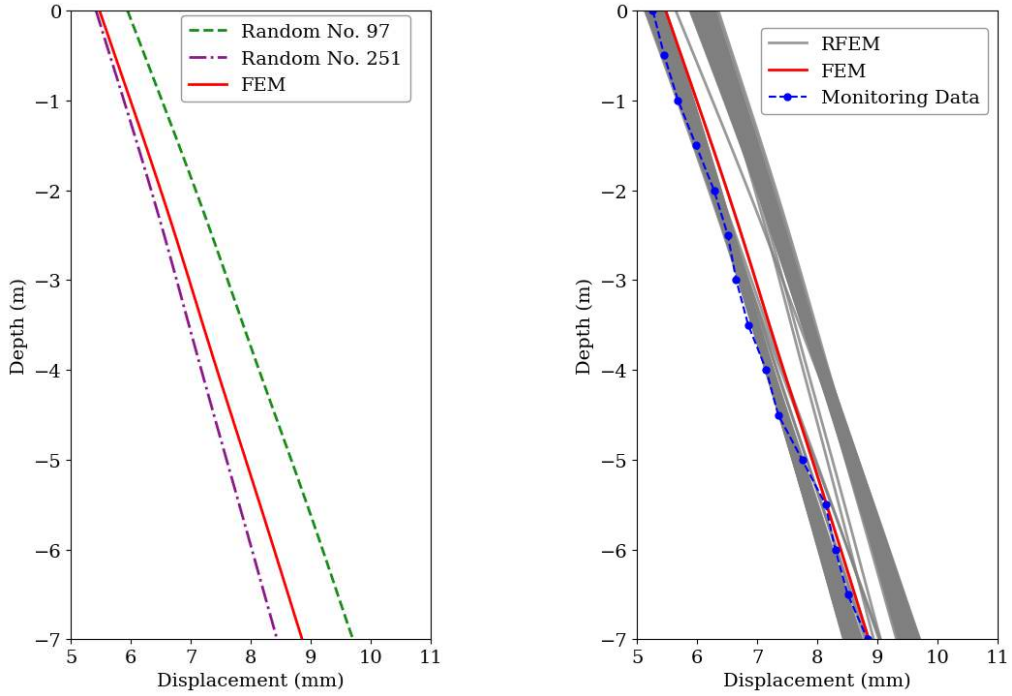
(a) Seed 97



(b) Seed 251

Fig. 12 Representative spatial distributions of E_{50} for the random-field realizations corresponding to (a) the maximum displacement (Seed 97) and (b) the minimum displacement (Seed 251)

Fig. 13 compares the lateral displacement profiles obtained from RFEM and deterministic FEM with the field measurements at inclinometer P07. The deterministic analysis closely reproduces the measured displacement profile, with a maximum displacement of 8.86 mm compared with the observed value of 8.84 mm. In contrast, the RFEM results exhibit a range of displacement profiles associated with the 300 random-field realizations. The left plot shows the profiles corresponding to the maximum and minimum displacement cases among the 300 realizations, while the right plot presents the complete set of 300 RFEM displacement profiles together with the deterministic FEM result and field measurements. Many of the RFEM realizations predict larger displacements than the deterministic model, particularly toward the lower portion of the wall. This difference indicates that spatial variability in the stiffness of the CDM-improved ground can alter the wall response even when the mean material properties remain unchanged. While the deterministic model provides a close match to the measured response at the selected section, the RFEM simulations reveal the range of possible displacements associated with different spatial stiffness distributions under the adopted random-field assumptions.



(a) (b)

Fig. 13 Comparison of CDM retaining-wall displacement profiles from RFEM, deterministic FEM, and field measurements: (a) maximum and minimum RFEM realizations; and (b) all 300 RFEM realizations.

Fig. 14 presents the histogram of maximum lateral wall displacement from 300 RFEM realizations, together with a fitted two-component lognormal mixture. The results show two clusters around 8.5-8.6 mm and 9.5-9.6 mm, with relatively few observations between them. The mixture model was used to describe this distribution. The two clusters are a feature of the present simulation dataset; they do not, by themselves, demonstrate distinct deformation mechanisms or multiple equilibrium states. Further investigation is needed to determine how the stiffness fields and the resulting ground deformation contribute to the separation between the clusters.

Fig. 15 presents the exceedance probability of maximum lateral wall displacement as a function of the prescribed displacement threshold, calculated from 300 Monte Carlo simulations. The exceedance probability decreases with increasing threshold, with relatively sharp reductions near the two displacement clusters identified in **Fig. 14**. At the observed maximum displacement of 8.84 mm recorded at inclinometer P07, the exceedance probability is approximately 44.0%. This indicates that 44% of the simulated stiffness distributions produce maximum wall displacements exceeding the field measurement. The estimated exceedance probability is conditional on the adopted random-field parameters and should not be interpreted as a structural failure probability, because the observed displacement of 8.84 mm is a reference measurement rather than an established design limit.

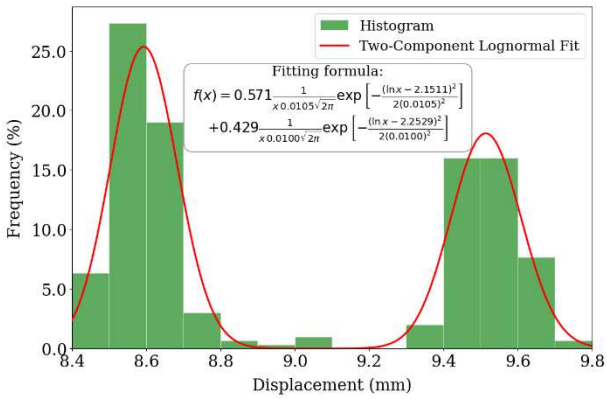


Fig. 14 Histogram of maximum lateral wall displacement from 300 Monte Carlo simulations and fitted two-component lognormal mixture.

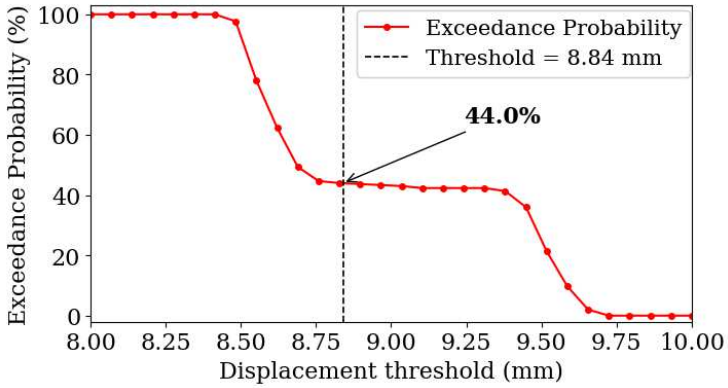


Fig. 15 Exceedance probability of maximum lateral wall displacement as a function of displacement threshold.

4.2. Effects of COV and scales of fluctuation (θ_x and θ_y)

A parametric analysis examined the effects of the COV of E_{50} and the prescribed horizontal and vertical scales of fluctuation of the underlying Gaussian field on CDM retaining-wall displacement. Six additional cases were considered, each varying one input parameter from its baseline value (**Table 5**). The mean E_{50} was fixed at 956.61 MPa. All cases used a lognormal stiffness distribution, an exponential autocorrelation function for the Gaussian field, and a 15.5 × 3.0 m domain divided into 0.5 × 0.5 m cells. In the COV comparisons, the Gaussian correlation parameters remained unchanged, although the normalized correlation of the resulting lognormal stiffness field changed with COV. These comparisons therefore include this correlation change alongside the change in stiffness variability. The baseline analysis used 300 Monte Carlo realizations, whereas each additional case used 50. The parametric results were used for exploratory comparisons of wall-displacement statistics and exceedance probabilities.

Table 5. Random-field parameter configurations for the baseline and parametric analyses.

Case	COV	θ_x (m)	θ_y (m)	Realizations
C0	0.53	7.0	1.4	300
C1	0.53	4.2	1.4	50
C2	0.53	9.8	1.4	50
C3	0.10	7.0	1.4	50
C4	0.30	7.0	1.4	50
C5	0.53	7.0	2.8	50
C6	0.53	7.0	3.5	50

Note: θ_x and θ_y denote the prescribed scales of fluctuation of the underlying Gaussian field.

Fig. 16 compares the lateral displacement profiles obtained from six random-field scenarios, each comprising 50 Monte Carlo realizations. Although the profiles exhibit a similar overall deformation pattern, their magnitudes and dispersion vary with the prescribed random-field parameters. These differences arise from variations in the spatial distribution of stiffness within the CDM-improved ground, which influence its contribution to the deformation resistance of the retaining system.

Increasing the COV from 0.1 to 0.3 produces a wider spread of displacement profiles (**Figs. 16c-d**). A higher COV increases the variability of local stiffness, allowing weaker and stiffer zones to develop within the improved ground. The location and extent of these zones can modify the deformation response, even when the mean modulus remains unchanged. The scales of fluctuation, in contrast, govern the spatial continuity of the stiffness field. Changes in the horizontal and vertical scale of fluctuation (**Figs. 16a-b** and **16e-f**) alter the predicted displacement profiles, but no consistent reduction in displacement dispersion is evident. This behavior is consistent with the competing effects of spatial correlation: extended low-stiffness zones may reduce the effective restraint provided by the improved ground, whereas more continuous high-stiffness zones may increase it. The resulting wall response therefore depends on both the magnitude of stiffness variability and the spatial arrangement of the generated modulus field.

The deterministic FEM prediction remains close to the field measurements, whereas the RFEM analyses produce a range of displacement responses under the same excavation conditions. This comparison illustrates a limitation of representing CDM-improved ground solely by its mean stiffness: different spatial distributions with identical statistical input parameters may produce different wall displacements. Quantitative comparison of the displacement statistics would be required to establish the relative influence of COV and scales of fluctuation.

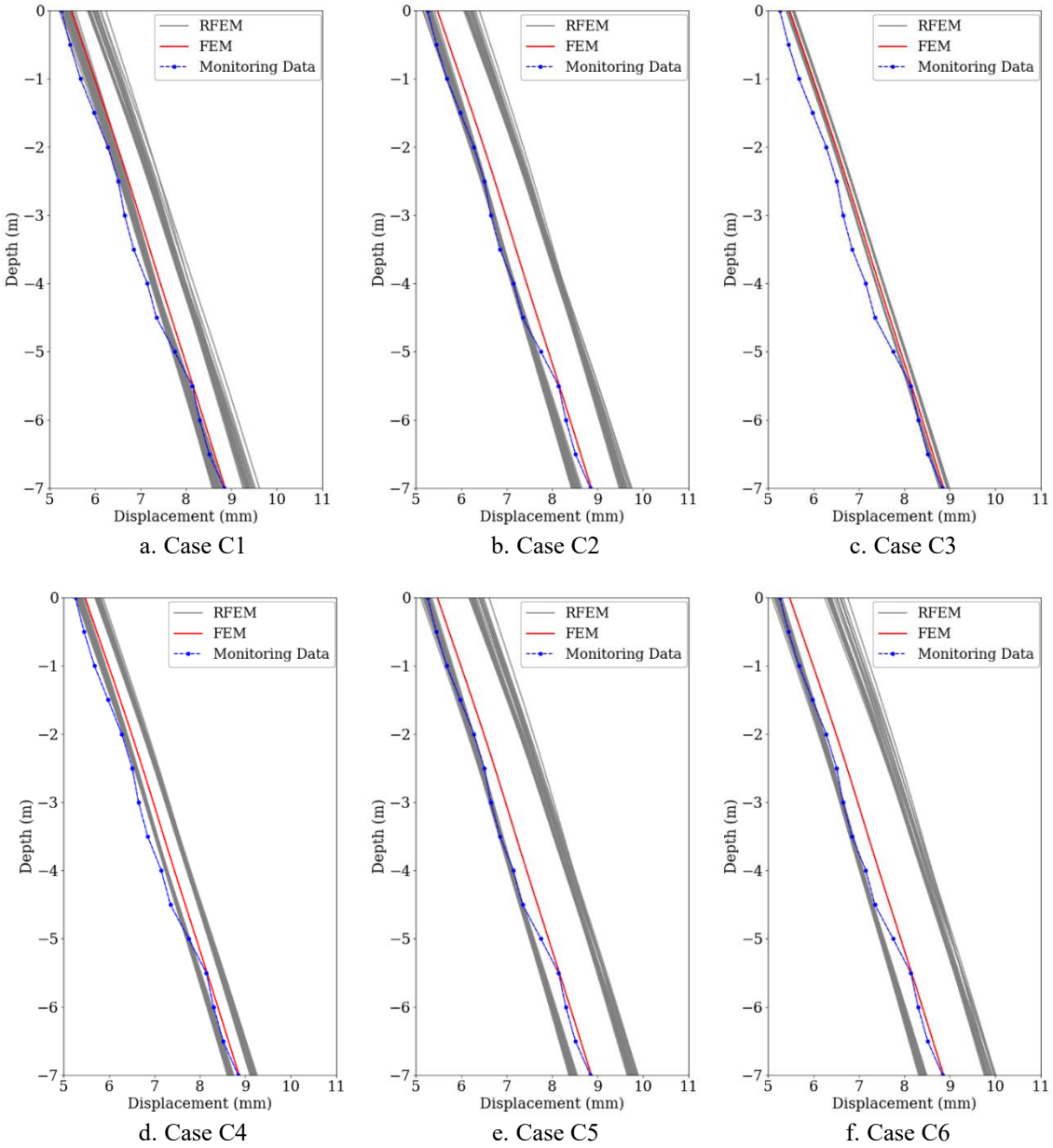


Fig. 16. Effects of random-field parameters on CDM retaining-wall displacement: (a-b) horizontal scale of fluctuation, (c-d) coefficient of variation, and (e-f) vertical scale of fluctuation.

Fig. 17 examines the influence of random-field parameters on the displacement-exceedance probability, using the maximum displacement measured at P07 (8.84 mm) as the reference threshold. The estimated probabilities range from 42% to 52% across the six scenarios. Increasing the horizontal scale of fluctuation from 4.2 to 9.8 m changes the exceedance probability from 50% to 48%, while increasing the vertical scale of fluctuation from 2.8 to 3.5 m changes it from 48% to 42%. For the COV scenarios, the corresponding probabilities are 52% and 48% at COV values of 0.1 and 0.3, respectively.

The influence of spatial variability on exceedance probability is not necessarily monotonic. Unlike displacement dispersion, which reflects the overall variability of the numerical response, exceedance probability depends on the proportion of simulated displacements lying above a particular threshold. An

increase in stiffness variability may broaden the displacement distribution without increasing the exceedance probability if a greater proportion of the simulated responses falls below the selected threshold. Similarly, changes in the scales of fluctuation modify the spatial arrangement of weak and stiff zones, but their effects on exceedance probability depend on the resulting displacement distribution. The relatively flat portions of the probability curves indicate intervals containing few simulated displacement values, illustrating the sensitivity of the estimated exceedance probability to the selected threshold.

Each parametric case comprised 50 realizations, meaning that a single exceedance changed the estimated probability by two percentage points. The observed probabilities ranged from 42% to 52%, with considerable overlap among the cases. These results do not provide sufficient evidence to establish a clear ranking of the effects of COV and the scales of fluctuation. Therefore, the estimates should be interpreted as exploratory findings, and larger sample sizes are needed to distinguish the differences more reliably.

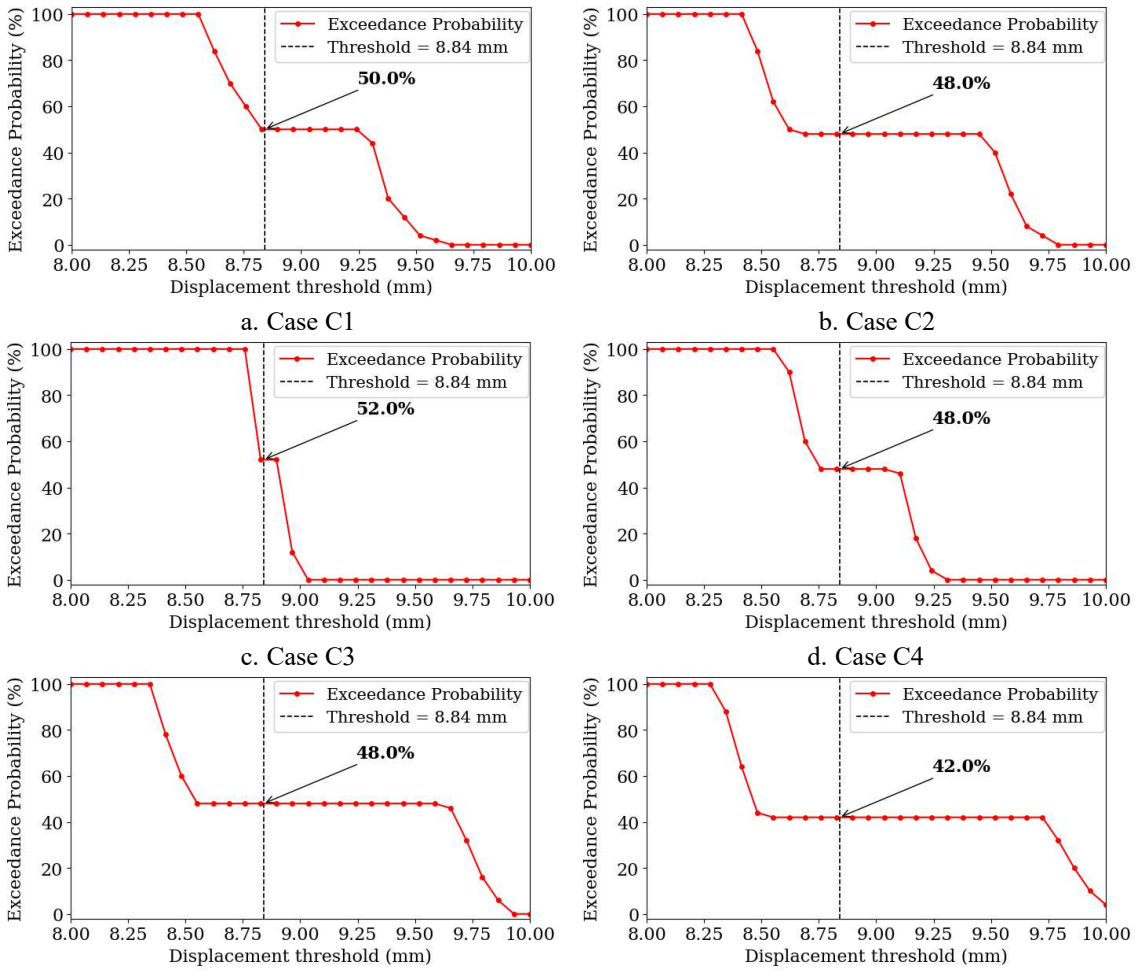


Fig. 17 Effects of random-field parameters on the exceedance probability of maximum lateral wall displacement: (a-b) horizontal scale of fluctuation, (c-d) coefficient of variation, and (e-f) vertical scale of fluctuation.

Table 6. Summary statistics of maximum lateral wall displacement for the baseline and parametric cases.

Case	N	Mean δ_{max} (mm)	SD (mm)	COV	P_{exc} at 8.84 mm (%)
C0	300	-	-	-	44.0
C1	50	9.03	0.37	4.04%	50.0
C2	50	9.03	0.55	6.06%	48.0
C3	50	8.88	0.09	0.97%	52.0
C4	50	8.91	0.26	2.93%	48.0
C5	50	9.08	0.67	7.37%	48.0
C6	50	9.01	0.74	8.19%	42.0

N is the number of RFEM realizations; SD is the sample standard deviation; P_{exc} at 8.84mm is the probability of exceeding the observed reference displacement of 8.84 mm.

Table 6 summarizes the mean, standard deviation, and COV of the maximum lateral wall displacement for the six random-field cases. Increasing the COV of E_{50} from 0.1 to 0.3 changes the mean displacement only slightly, from 8.877 to 8.905 mm, whereas the standard deviation increases from 0.085 to 0.26 mm. The corresponding displacement COV increases from 0.97% to 2.93%. For these two cases, the threefold increase in the input COV is accompanied by an approximately threefold increase in the standard deviation of displacement, suggesting a stronger effect on response dispersion than on the mean. The confidence intervals for the parametric cases overlap substantially. The estimated exceedance probabilities of 42-52% therefore do not establish a statistically reliable ranking of parameter effects. With 50 realizations per case, these comparisons remain exploratory.

Changes in the scales of fluctuation also affect displacement dispersion. Increasing θx from 4.2 to 9.8 m increases the standard deviation from 0.37 to 0.55 mm, while the mean remains approximately 9.03 mm. Increasing θ_y from 2.8 to 3.5 m increases the standard deviation from 0.67 to 0.74 mm and slightly reduces the mean from 9.077 to 9.011 mm. Within the investigated parameter ranges, changes in both COV and the scales of fluctuation are associated with greater differences in displacement dispersion than in the mean response. These trends should be interpreted cautiously because each parametric case comprises 50 realizations.

The results are conditional on the adopted equivalent-continuum representation. The two-dimensional model does not explicitly represent the three-dimensional column arrangement, relative movement between columns and surrounding soil, or local failure of individual columns. The variability measured in CDM specimens was transferred directly to the equivalent composite stiffness without additional spatial averaging at the composite scale. These assumptions limit the extent to which the predicted displacement distributions can represent the behavior of the actual column-soil system.

The equivalent undrained shear strength was held constant while stiffness varied spatially. The analyses therefore isolate the effect of stiffness variability under fixed-strength conditions and do not account for variability in strength or its correlation with stiffness.

The equivalent stiffness was based on the CDM secant modulus measured in unconfined compression tests at a curing age of 28 days. Stress-dependent stiffness and changes associated with curing age were not explicitly modeled. Furthermore, the linear elastic wall model does not assess tensile cracking or material failure. The results therefore describe displacement responses under the adopted stiffness assumptions and should not be interpreted as a verification of the structural safety of the CDM wall.

The findings provide insights into the effects of spatial stiffness variability on retaining-wall displacement under the investigated conditions. Further investigations involving additional field monitoring data, larger stochastic simulation samples, and different ground conditions and CDM configurations would help extend the applicability of the present approach to a broader range of deep excavation projects.

5. CONCLUSION

This study examined the effect of spatial variability in CDM base stiffness on retaining-wall displacement using RFEM. The numerical model was calibrated against the displacement profile measured at P07. The analyses included 300 baseline realizations and six parametric cases with 50 realizations each. The following conclusions were drawn:

(1) Spatial variability in base stiffness produced a range of wall displacements while wall properties and material strengths remained unchanged. The baseline results formed two clusters around 8.5-8.6 mm and 9.5-9.6 mm. A two-component lognormal mixture described this distribution. These clusters do not establish distinct deformation mechanisms or multiple equilibrium states; their physical or numerical origin requires further investigation.

(2) Increasing the COV of E_{50} from 0.1 to 0.3 increased the displacement standard deviation from 0.085 to 0.26 mm. The mean changed only slightly, from 8.877 to 8.905 mm. Changes in the scales of fluctuation also affected dispersion. Increasing θ_x from 4.2 to 9.8 m increased the standard deviation from 0.37 to 0.55 mm, while the mean remained approximately 9.03 mm. Increasing θ_y from 2.8 to 3.5 m increased the standard deviation from 0.67 to 0.74 mm. Within these comparisons, changes in the random-field parameters affected dispersion more than the mean response. The results do not establish a general ranking of parameter influence.

(3) The estimated probability of exceeding the measured displacement of 8.84 mm was approximately 44% for the baseline case and 42-52% for the parametric cases. These probabilities are conditional on the adopted modeling assumptions and represent exceedance of a field measurement, not structural failure or violation of a design limit. With 50 realizations per parametric case, the differences are insufficient to establish a statistically reliable ranking of exceedance probabilities.

(4) The RFEM results complement the deterministic prediction by describing displacement variability under the prescribed stiffness fields. Their interpretation is limited by the two-dimensional equivalent-continuum model, fixed material strengths, and direct transfer of specimen variability to composite stiffness. Further work should examine the origin of the two displacement clusters, spatial averaging at the composite scale, and the joint variability of CDM stiffness and strength.

Competing interests

The authors declare no competing interests.

Data availability

The datasets generated and analyzed during the current study are available from the corresponding author upon reasonable request.

REFERENCES

1. Shao Y, Macari EJ, Cai W. Compound deep soil mixing columns for retaining structures in excavations. J Geotech Geoenviron Eng. 2005;131(11):1370-1377. doi:10.1061/(ASCE)1090-0241(2005)131:11(1370).
2. Jamsawang P, Voottipruex P, Jongpradist P, Bergado DT. Parameters affecting the lateral movements of compound deep cement mixing walls by numerical simulations and parametric analyses. Acta Geotech. 2015;10(6):797-812. doi:10.1007/s11440-015-0417-5.
3. Jamsawang P, Jamnam S, Jongpradist P, Tanseng P, Horpibulsuk S. Numerical analysis of lateral movements and strut forces in deep cement mixing walls with top-down construction in soft clay. Comput Geotech. 2017;88:174-181. doi:10.1016/j.compgeo.2017.03.018.
4. Voottipruex P, Jamsawang P, Sukontasukkul P, Jongpradist P, Horpibulsuk S, Chindaprasirt P. Performances of SDCM and DCM walls under deep excavation in soft clay: field tests and 3D simulations. Soils Found. 2019;59(6):1728-1739. doi:10.1016/j.sandf.2019.07.012.
5. Waichita S, Jongpradist P, Schweiger HF. Numerical and experimental investigation of failure of a DCM-wall considering softening behaviour. Comput Geotech. 2020;119:103380. doi:10.1016/j.compgeo.2019.103380.
6. Chen EJ, Liu Y, Lee FH. A statistical model for the unconfined compressive strength of deep-mixed columns. Géotechnique. 2016;66(5):351-365. doi:10.1680/jgeot.14.P.162.
7. Wijerathna M, Liyanapathirana DS. Reliability-based performance of embankments improved with deep mixing considering spatial variability of material properties. ASCE-ASME J Risk Uncertainty Eng Syst Part A Civ Eng. 2018;4(4):04018035. doi:10.1061/AJRUA6.0000987.
8. Pan Y, Shi G, Liu Y, Lee FH. Effect of spatial variability on performance of cement-treated soil slab during deep excavation. Constr Build Mater. 2018;188:505-519. doi:10.1016/j.conbuildmat.2018.08.112.
9. Phoon KK, Kulhawy FH. Characterization of geotechnical variability. Can Geotech J. 1999;36(4):612-624. doi:10.1139/t99-038.
10. Luo Z, Hu B, Wang Y, Di H. Effect of spatial variability of soft clays on geotechnical design of braced excavations: a case study of Formosa excavation. Comput Geotech. 2018;103:242-253. doi:10.1016/j.compgeo.2018.07.020.
11. Zhang W, Han L, Gu X, Wang L, Chen F, Liu H. Tunneling and deep excavations in spatially variable soil and rock masses: a short review. Undergr Space. 2022;7(3):380-407. doi:10.1016/j.undsp.2020.03.003.
12. Nguyen HH, Le TN. Numerical analysis of diaphragm wall behavior in a jet-grouted deep excavation: a random field case study. Sci Rep. 2026;16:25332. doi:10.1038/s41598-026-56123-2.
13. Coteccons Construction Joint Stock Company. Construction documentation for the Riviera Point mixed-use development, Phase 1C (Ho Chi Minh City, 2023).
14. Schanz T, Vermeer PA, Bonnier PG. The Hardening Soil Model: formulation and verification. In: Beyond 2000 in Computational Geotechnics: 10 Years of PLAXIS. Balkema; 1999:281-296. doi:10.1201/9781315138206-27.
15. Lim A, Ou CY, Hsieh PG. Evaluation of clay constitutive models for analysis of deep excavation under undrained conditions. J GeoEng. 2010;5(1):9-20. doi:10.6310/JOG.2010.5(1).2.
16. Bui LM, Wu L, Cheng Y, Dong DJ. Evaluation of using hardening soil model for predicting wall deflections caused by deep excavation: A case study at the Ho Chi Minh metro line 1, Vietnam. Archives of Civil Engineering. 2024;70(1):357–373. doi:10.24425/ace.2024.148916.

17. Nguyen ND, Tran TD. Phân tích ngược hiệu chỉnh thông số độ cứng nền đất yếu bằng mô hình Hardening Soil cho bài toán hố đào sâu tại Thành phố Hồ Chí Minh. HCMCOU J Sci Eng Technol. 2026;21(1):3–20. https://doi.org/10.46223/HCMCOUJS.tech.vi.21.1.4510.2026.
18. NIST/SEMATECH. e-Handbook of Statistical Methods. National Institute of Standards and Technology; 2012. doi:10.18434/M32189.
19. Fenton GA, Griffiths DV. Risk Assessment in Geotechnical Engineering. John Wiley & Sons; 2008. doi:10.1002/9780470284704.
20. Federal Highway Administration. Federal Highway Administration Design Manual: Deep Mixing for Embankment and Foundation Support. Report No. FHWA-HRT-13-046. US Department of Transportation; 2013.
21. Rashid ASA, Bunawan AR, Mat Said KN. The deep mixing method: bearing capacity studies. Geotech Geol Eng. 2017;35(4):1271-1298. doi:10.1007/s10706-017-0196-x.
22. Gan X, Liu N, Bezuijen A, Gong X. Random responses of shield tunnel to new tunnel undercrossing considering spatial variability of soil elastic modulus. Appl Sci. 2024;14(9):3949. doi:10.3390/app14093949.
23. Shinozuka M, Deodatis G. Simulation of stochastic processes by spectral representation. Appl Mech Rev. 1991;44(4):191-204. doi:10.1115/1.3119501.
24. Le DV, Nguyen KT. Effect of spatial variability of soil shear strength on the displacement of an axially loaded pile. Civil Eng J. 2026;12(3):866-881. doi:10.28991/CEJ-2026-012-03-02.
25. Zhang Y, Zhang Z, Liu S, Gao M, Wang J, Cao J. Probabilistic analysis of ground settlement induced by soil and rock composite foundation excavation considering spatial variability. Sci Rep. 2025;15:16152. https://doi.org/10.1038/s41598-025-00370-2.
26. Nguyen TS, Ngamcharoen K, Likitlersuang S. Statistical characterisation of the geotechnical properties of Bangkok subsoil. Geotech Geol Eng. 2023;41(3):2043-2063. doi:10.1007/s10706-023-02390-z.
27. Haldar S, Babu GLS. Effect of soil spatial variability on the response of laterally loaded pile in undrained clay. Comput Geotech. 2008;35(4):537-547. doi:10.1016/j.compgeo.2007.10.004.
28. Vanmarcke EH. Probabilistic modeling of soil profiles. J Geotech Eng Div. 1977;103(11):1227-1246. doi:10.1061/AJGEB6.0000517.
29. Stuedlein AW, Kramer SL, Arduino P, Holtz RD. Geotechnical characterization and random field modeling of desiccated clay. J Geotech Geoenviron Eng. 2012;138(11):1301-1313. doi:10.1061/(ASCE)GT.1943-5606.0000703.